Supplementary Information

Blocking Multifaceted Degradation Pathways via Fluorinated Hydrogen-Bond Armor for Stable Perovskite Solar Cells

Yilin Gao,†[ab] Yuehui Li,†[a] Guozhen Liu,*[a] Naitian Zhang,[c] Siao Li,[a] Zhiyong Wang ,[a] Zheng Lv,[a] Yinjuan Zhang,[a] Lin Yang,[a] Jie Zhang,[a] Linghui Zhang,[d] Wenrui Li,[a] Wenming Tian,[d] Wenzhe Li,[e] Zhehan Ying,[f] Jijun Qiu,[b] and Yantao Shi*[a]

[a] State Key Laboratory of Fine Chemicals, School of Chemistry, Frontier Science Center for Smart Materials, Dalian University of Technology, Dalian 116024, P. R. China

E-mail: gzliu@dlut.edu.cn, shiyantao@dlut.edu.cn

[b] School of Integrated Circuits, Dalian University of Technology, Dalian 116024, P. R. China

[c] College of Pharmacy, Jiamusi University, Jiamusi 154007, P. R. China

[d] State Key Laboratory of Chemical Reaction Dynamics, Dalian Institute of Chemical Physics, Chinese Academy of Sciences, Dalian 116023, China

[e] Institute of New Energy Technology, College of Physics & Optoelectronic Engineering, Jinan University, Guangzhou 510632, P. R. China

[f] Materials Characterization and Preparation Facility, The Hong Kong University of Science and Technology, Guangzhou 511453, P. R. China

† These authors contributed equally.

Experimental Section

Materials

Methylammonium iodide (CH_3NH_3I, MAI, 99.5%), formamidine hydroiodide ($HC(NH_2)_2I$, FAI, 99.5%), methylammonium chloride (MACl, 99.5%), cesium iodide (CsI, 99.999%), phenyl-C61-butyric acid methyl ester (PC61BM, 99.9%), and bathocuproine (BCP, 96%) were purchased from Xi'an Yuri Solar Co., Ltd. PbI_2 (99.999%) was purchased from Advanced Election Technology Co., Ltd. [4-(3,6-Dimethyl-9H-carbazol-9-yl)butyl]phosphonic Acid (Me-4PACz, >99.0%) and [2-(3,6-Dimethoxy-9H-carbazol-9-yl)ethyl]phosphonic Acid (MeO-2PACz, >98.0%) were purchased from TCI America. Anhydrous dimethyl sulfoxide (DMSO, 99.9%), anhydrous dimethylformamide (DMF, 99.8%), isopropanol (IPA, 99.8%), and chlorobenzene (CB, 99.8%) were all purchased from Sigma-Aldrich. 2-Mercaptobenzimidazole (MBI, 99%), 2-Mercapto-5-Methoxybenzimidazole (CH_3O-MBI, 99%), 6-Chloro-1H-Benzo[D]Imidazole-2-Thiol (Cl-MBI, 99%) and 6-Fluoro-1H-Benzimidazole-2-Thiol (F-MBI, 97%) were purchased from Adamas. Au (99.999%) and Ag (99.999%) were purchased from Zhong Nuo Advanced Material (Beijing) Technology Co., Ltd. Fluorine-doped tin dioxide (FTO, 7 Ω sq^{-1}) and Indium-doped tin oxide (ITO, 12 Ω sq^{-1}) glasses were purchased from Suzhou Shangyang Solar Energy Technology Co., Ltd. All reagents and substrates were used as received without further purification.

Device Fabrication

FTO substrates were cleaned by sequential ultrasonication in deionized water, ethanol, and isopropanol (15 min each), and subsequently subjected to UV–ozone treatment for 15 minutes. After cooling to room temperature, the substrate was transferred to a nitrogen-filled glove box. The MeO-2PACz and Me-4PACz mixture (0.5 mg mL^{-1} in IPA) was spin-coated on the FTO at 4000 rpm for 30 s and annealed at 100 °C for 10 min. Then, the substrate was washed by isopropyl alcohol to remove residual self-assembly molecules. The perovskite layer was spin-coated on the substrate by one-step deposition method. The 1.5

M perovskite precursor solution with the composition of $Cs_{0.05}FA_{0.85}MA_{0.1}PbI_3$ was prepared by fully dissolving FAI, MAI, CsI, PbI_2 in a mixed solvent of DMF and DMSO with a stochiometric ratio of 4:1 (v/v). An additional 5 mol % PbI_2 and 10 mol % MACl were added to the precursor to achieve better crystallization. For MBI and F-MBI modified samples, an additional 5 mg mL^{-1} of MBI/F-MBI additive was added to the perovskite precursor solution. The solution was stirred at room temperature until fully dissolved, and then filtered through a 0.22 μm polytetrafluoroethylene (PTFE) membrane prior to use. A volume of 70 μL perovskite precursor solution was deposited onto substrates coated with a mixed layer of MeO-2PACz and Me-4PACz, followed by spin-coating at 5000 rpm for 50 s and 150 μL of chlorobenzene was dropped onto the spinning substrate during the final 10 s of spin-coating. The resulting films were immediately transferred to a hotplate and annealed at 100 °C for 30 minutes. Subsequently, a saturated solution of PDI in IPA was spin-coated onto the perovskite film at 5000 rpm for 30 s, followed by thermal annealing at 100 °C for 10 minutes. Then, a PCBM layer (20 mg mL^{-1} in CB) was spin-coated onto the substrate at 1500 rpm for 30 s, followed by the deposition of a BCP layer via spin-coating at 5000 rpm. Finally, a 150 nm thick Ag back electrode was thermally evaporated through a shadow mask (defining an active area of 0.049 cm^2) under a vacuum of 4×10^{-5} Pa.

Large-area modules Fabrication

The FTO glass substrates (12 Ω sq^{-1}, 10 × 10 cm^2) were cleaned using the same procedure as previously described, followed by UV–ozone treatment for 20 minutes. The mixed solution of MeO-2PACz and Me-4PACz (1 mg mL^{-1} in ethanol) was blade-coated onto the FTO substrate at a speed of 10 mm s^{-1} under ambient conditions (20-40% RH, room temperature), followed by thermal annealing at 110 °C for 5 minutes. After cooling to room temperature, the perovskite precursor solution (1.2M, $Cs_{0.05}FA_{0.95}PbI_3$) was prepared by dissolving PbI_2, MACl, CsI, and FAI in a mixed solvent of 6 mL DMF and 1 mL NMP, along with 0.5 mg mL^{-1} F-MBI, under constant stirring. The perovskite films were fabricated via blade

coating onto the substrates at a speed of 10 mm s^{-1} with a 200 μm gap, under ambient conditions (20-40% RH, room temperature). The wet films were subsequently subjected to vacuum-assisted crystallization at 2.6 Pa for 1 minute, followed by thermal annealing in air at 120 °C for 20 minutes. Finally, the solar cell modules were completed by sequential thermal evaporation of C_{60} (25 nm, 0.4 Å s^{-1}), BCP (5 nm, 0.2 Å s^{-1}), and Cu (250 nm, 3 Å s^{-1})[1].

Series-parallel interconnection of subcells in perovskite modules was achieved via established laser scribing techniques. The resulting large-area module featured an active area of 64.48 cm^2 and was fabricated on a P1 pre-patterned FTO glass substrate with a P1 line width of 40 μm. Each sub cell was 7.5 mm wide, with P2 and P3 scribe widths of approximately 35 and 30 μm, respectively (**Figure S21**). A total of 11 subcells were connected to form the complete module. The total width of non-active areas was ~150 μm, corresponding to a geometric fill factor (GFF) of 98%.

Characterization

Characterization of Materials

UV-visible absorption spectra related to the interactions between FAI and additive molecules, as well as those of the perovskite films, were recorded using a UV-vis spectrophotometer (UV-3600 Plus, Shimadzu, Japan). The in-situ MS experimental setup included a gas delivery system, a stainless steel photoreactor with quartz windows, a Xe light source system providing light in the range of 300 nm to 1000 nm, and an in-situ MS (GSD301O3, Pfeiffer Vacuum, Germany) equipped with an electron ionization (EI) ion source. The ionization voltage of the EI source was set to 70 eV in accordance with standards from the National Institute of Standards and Technology (NIST). Fourier-transform infrared (FTIR) spectroscopy was employed to investigate the interactions between FAI and the additive molecules (MPA, Bruker, Germany). The hydrogen-bonding interactions between FA^+ and the additive molecules were investigated by ^1H NMR spectroscopy, conducted using an AVANCE NEO 600 MHz

spectrometer (Bruker, Switzerland). The crystallinity of perovskites was tested by an X-ray diffractometer (XRD, D8 ADVANCE, Bruker, Germany). The electronic and atomic structures of thin film were characterized using an ESCALAB 250Xi photoelectron spectrometer (Thermo Fisher Scientific, USA). Ultraviolet photoelectron spectroscopy (UPS) was employed to characterize the valence electronic states and band structure at both the surface and buried interfaces of thin films. X-ray photoelectron spectroscopy (XPS) was employed to determine the elemental composition, chemical states, and relative concentrations of species at the material surface. The surface and cross-sectional morphologies were tested by field emission scanning electron microscopy (FE-SEM, Hitachi, SU88220, Japan). The surface topography of the perovskite film was characterized using atomic force microscopy (AFM, JPK Nanowizard 4XP, Bruker, Germany, tap mode, RTESPA-300), and the surface roughness was quantitatively analyzed from the obtained images. In addition, the surface contact potential information of perovskite film was tested by KPFM (tap mode, SCM-PIC-V2) modules in AFM. In situ XRD measurements were performed using the Dandong Tongda TL-10M XRD, integrated with the TMTD temperature control system, in continuous scanning mode. The scan covered a 2-theta range from 5-45° with a step size of 0.02° and an exposure time of 0.4 seconds, taking approximately 8 min to complete a full cycle. Stable photoluminescence (PL) and time-resolved photoluminescence (TRPL) spectra were measured by a fluorescence spectrometer (Edinburgh, FLS1000, U.K.). Two-dimensional PL and TRPL imaging of the perovskite films was performed using a custom-built microscope equipped with a time-correlated single-photon counting (TCSPC) module. The system consisted of a high-speed detector (MPD, PicoQuant, Germany), a 100 oil immersion objective (NA = 1.4, Olympus UPlanSApo), and a pulsed laser source (LDH-P-C-405, PicoQuant, Germany). ToF-SIMS was conducted to evaluate the depth distributions of Cs^+, $CH_5N_2^+$, Pb+, F^- and InO_2^- ions in the perovskite layer. The films were tested using (ION-TOF M6 Hybrid). A pulsed 30 keV Bi^{3+} (0.80 pA pulse current) ion beam set in spectrometry

mode was applied for depth profiling. The typical analyzed area was 200 × 200 μm^2. Large Arn$^+$ cluster ions (with n ~ 1500 Ar atoms per cluster) with a bombarding energy of 10 keV was used for sputtering of the samples with a typical sputtered area of 600 × 600 μm^2.

Device Characterization

The current density-voltage (*J-V*) curves of the device is measured under AM 1.5G illumination at 100 mW cm^{-2} (calibrated with a standard Si solar cell) using a source measurement unit (SMU) instrument (2400, Keithley's Series, USA). The intensity was calibrated using an ISO-17025 standard calibrated reference silicon cell (91150V-KG3, Newport, USA). External quantum efficiency (EQE) spectra were measured using a quantum efficiency measurement system (QE-R, Enlitech, China). Electrochemical impedance spectroscopy (EIS), Mott–Schottky analysis, and transient photovoltage decay (TPV) were performed under dark conditions using an electrochemical workstation (Zennium, Zahner, Germany).

Stability of Perovskite films and Solar Cells

To evaluate the effect of the "precise shielding" strategy on the UV stability of perovskite films, surface characterization was conducted after exposing the glass/FTO/ETL/perovskite structure to continuous ultraviolet irradiation (365 nm, 35 mW cm^{-2}) for 5 hours. During the test, the substrate temperature was maintained at approximately 40 °C, with a relative humidity of 25 ± 10%. During this process, scanning electron microscopy (SEM) was employed to monitor the morphological evolution of the perovskite film surface after 0 and 5 hours of UV irradiation. Under stronger ultraviolet irradiation at 365 nm (intensity = 60 mW cm^{-2}, substrate temperature ~ 45 °C, relative humidity ~ 18%), the structural evolution of the perovskite films was monitored by in situ X-ray diffraction (XRD).

The long-term operational stability of the unencapsulated perovskite solar cells was evaluated in a nitrogen-filled glovebox using a photovoltaic light soaking test system (PVLT-6001M-16A PV, Suzhou Deray Instruments Co., Ltd., China). To evaluate the thermal stability of the perovskite devices, thermal

aging was conducted at 85 °C under an inert N_2 atmosphere, and the evolution of the power conversion efficiency (PCE) was continuously monitored.

Calculation Methods

Note 1: Carrier recombination lifetime and exciton lifetime calculation

The carrier recombination lifetimes were extracted from time-resolved photoluminescence (TRPL) measurements by fitting the decay curves with a bi-exponential function:

$$y\,(t) = A_1 exp^{\frac{-t}{\tau_1}} + A_2 exp^{\frac{-t}{\tau_2}} + y_0$$

$$\tau_{ave} = \frac{\sum A_i \tau_i^2}{\sum A_i \tau_i}$$

where A_1 and A_2 are the relative amplitudes, τ_1 and τ_2 correspond to the fast and slow decay components, which are associated with nonradiative recombination at surface trap states near grain boundaries and radiative recombination within the bulk perovskite film, respectively.

Note 2: Calculation of activation energy of ionic migration (E_a^{ion})[2]

The conductivity of perovskite film at different temperatures was firstly calculated by equation:

$$\sigma = \frac{I}{V} \times \frac{d}{S}$$

where d and S are the thickness and area of perovskite film, then, from equation:

$$\ln\,(\sigma T) = \frac{E_a^{ion}}{kT} + ln\sigma_0$$

it can be concluded that the first stage slope in Figure 3f is $\frac{E_a^{ion}}{k}$, where k is the Boltzmann constant, so that E_a^{ion} can be figured out.

Note 3: Residual stress analysis by GIXRD[3]

For GIXRD measurement, the (210) plane of perovskite, corresponding to a diffraction peak at 31.6°, was selected as the stress-free reference due to its capability to provide more reliable information on structural

symmetry. During the measurement, 2θ is fixed while the instrument tilt angles (ψ) were varied to control the X-ray penetration depth. The ψ were fixed at 5°, 15°, 25°, 35°, and 45°, respectively. According to Bragg's Law and generalized Hooke's Law, the relationship of 2θ-$\sin^2\psi$ can be given by the following equation:

$$\sigma = -\frac{E_p}{(1+\nu_p)}\frac{\pi}{180^\circ}cot\theta_0\frac{\partial(2\theta)}{\partial[(sin\Psi)^2]}$$

where E_p is the perovskite modulus (10 GPa) and v_p is Poisson's ratio of the perovskite (0.3). θ_0 represents half of the stress-free scattering angle ($2\theta_0$ = 31.6°). The residual stress in the perovskite films is determined by fitting the 2θ as a function of $\sin^2\psi$, and the slope of the fitted line represents the scale of the residual strain. The negative slope indicates the films bear tensile stress, while the positive slope indicates the films bear compressive stress.

Note 4: Analyzation of space-charge-limited current (SCLC) model

The dark *J-V* characteristics can be divided into three distinct regions: (I) the Ohmic region at low bias region, (II) the trap-filled limited region (TFL) at intermediate bias region, and (III) a trap-free SCLC region at high bias region. In the TFL region, as the applied voltage increases, the trap states are progressively filled until all traps are occupied at the trap-filled limit voltage (V_{TFL}). The trap density can be calculated using the following equation:

$$N_t = \frac{2\varepsilon\varepsilon_0 V_{TFL}}{qL^2}$$

Where N_t represents the trap density, ε denotes the dielectric constants of the perovskite material, ε_0 is the vacuum permittivity, L refers to the thickness of the perovskite film, and q is the elementary charge. V_{TFL} is obtained by fitting the dark *I-V* data with the equation.

Note 5: The dependence of J_{sc} and V_{oc} of the PSCs on light intensity

The ideality factor nKT/q can be calculated by equation:

$$V_{oc} = \frac{nKT}{q} ln(P_{light})$$

The exponential factor α can be calculated by equation:

$$\alpha = \frac{ln(J_{sc})}{ln(P_{light})}$$

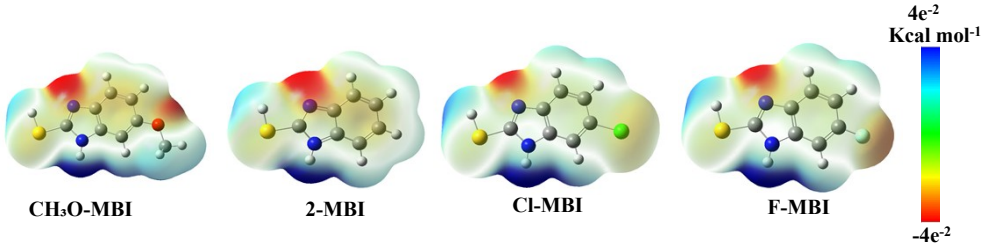

Fig. S1 The distribution of electrostatic potential (ESP) of R-MBIs (R= CH_3O, H, Cl, and F).

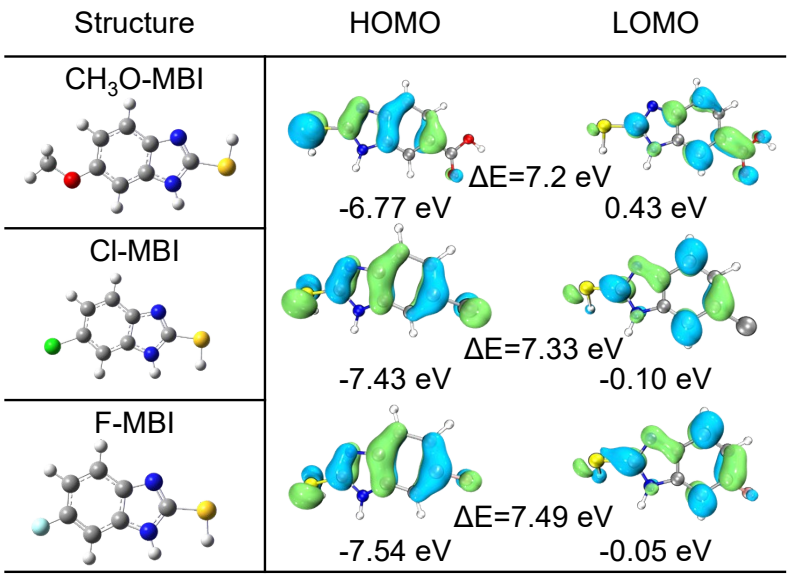

Fig. S2 Frontier molecular orbitals of individual additive molecules.

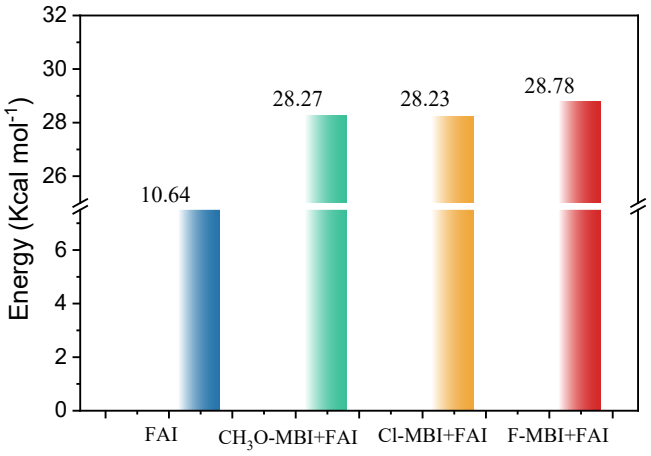

Fig. S3 The proton dissociation energies (PDEs) at the same N–H site were calculated for FAI and FAI+R-MBI composite systems (R = CH_3O, Cl, and F).

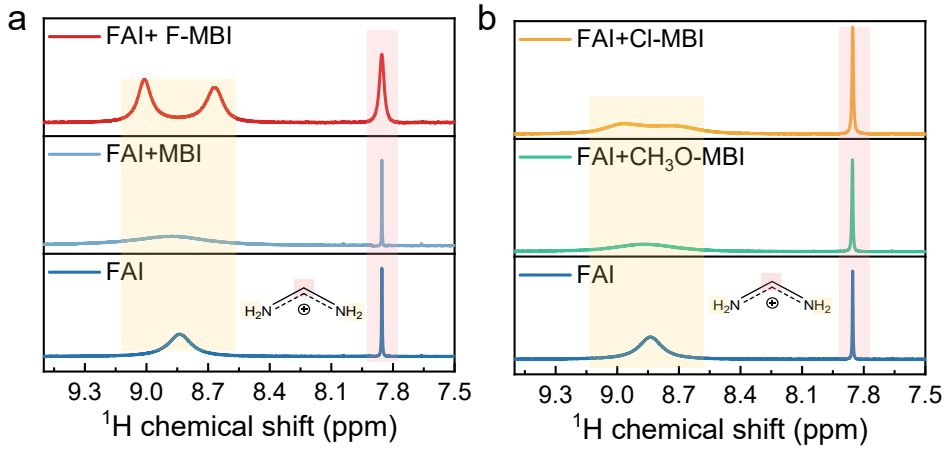

Fig. S4 (a) ^{1}H NMR spectra of neat FAI, FAI+MBI and FAI+F-MBI solutions. (b) ^{1}H NMR spectra of neat FAI, FAI+CH_3O-MBI and FAI+Cl-MBI solutions. The solvent is dimethyl sulfoxide-d_6 (DMSO-d6).

Since the hydrogen bonding interactions between FA^+ and the additive molecules involve a dynamic equilibrium between formation and dissociation, weak interactions—as in the case of MBI—are less likely to be captured during NMR measurements. As a result, the ^{1}H NMR spectrum exhibits a single, broadened resonance with a slight chemical shift, reflecting an averaged environment rather than distinct binding states. In contrast, when the hydrogen bonding interactions between F-MBI and FA^+ are stronger and more stable, the exchange dynamics slow down, making the interactions less reversible on the NMR timescale. As a result, peak splitting is observed, indicating the presence of two distinct chemical environments.[4–6]

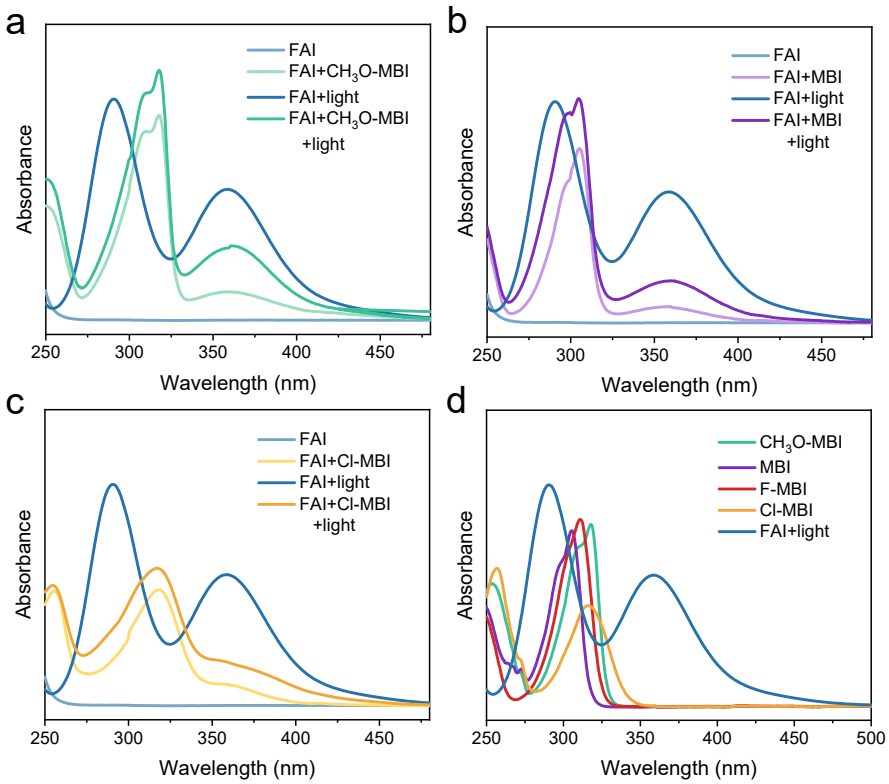

Fig. S5 UV-Vis absorption spectra of different aging solutions. (a) UV-Vis absorption spectra of FAI/IPA and (FAI+CH_3O-MBI)/IPA solutions before and after light aging. (b) UV-Vis absorption spectra of FAI/IPA and (FAI+MBI)/IPA solutions before and after light aging. (c) UV-Vis absorption spectra of FAI/IPA and (FAI+Cl-MBI)/IPA solutions before and after light aging. (d) UV-Vis absorption spectra of CH_3O-MBI/IPA, MBI/IPA, F-MBI/IPA and COOH-MBI/IPA solutions.

The suppression of I_3^- formation was systematically evaluated by introducing additive molecules with various substituents. MBI, possessing inherent reductive capability due to its -SH group, led to a decrease in I_3^- content compared to the pristine FA^+ solution, indicating its ability to partially reduce photo-oxidized I_2 back to I^-.[7] However, the introduction of functional substituents capable of forming hydrogen bonds significantly strengthened the interaction with FA^+. Among the other additives studied, CH_3O-MBI exhibited the weakest suppression effect, not only due to its limited electronegativity and relatively weak hydrogen bonding with FA^+, but also the electron-donating nature of the methoxy group reduced the overall reductive capacity of the molecule, thereby hindering its ability to effectively stabilize the cation

and suppress the oxidation of I^-. In contrast, Cl-MBI showed improved performance, benefiting from the stronger electron-withdrawing nature of the -Cl group, which enhanced hydrogen bond interactions and cation stabilization. Notably, F-MBI demonstrated the most effective inhibition of I_3^- generation, as the highly electronegative -F substituent strengthened the hydrogen bond interaction, leading to more efficient passivation of FA^+ and reduction of I_2. These findings suggest that both the reductive functionality and the strength of hydrogen bonding-tuned by substituent electronegativity-synergistically contribute to the stabilization of iodide species and suppression of I_3^- formation.

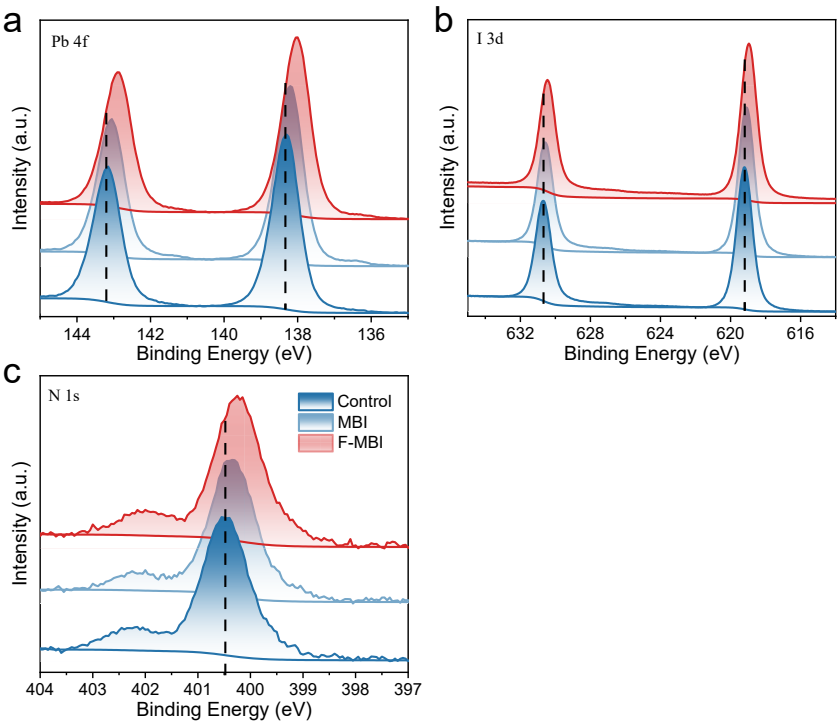

Fig. S6 XPS spectra of (a) Pb 4f, (b) I 3d, and (c) N 1s of control, MBI and F-MBI modified perovskite films.

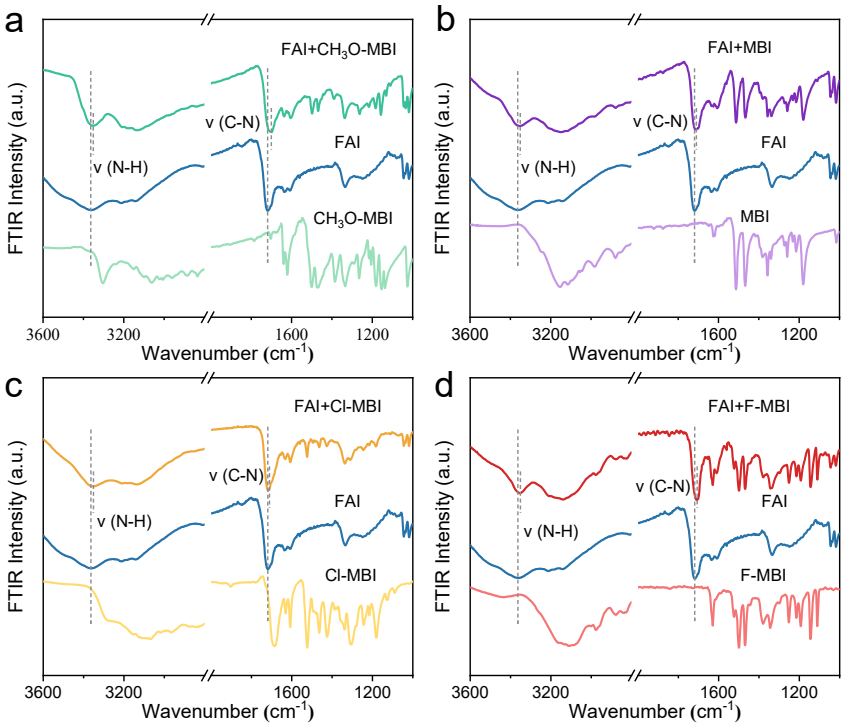

Fig. S7 FTIR spectra for (a) CH_3O-MBI, FAI, and FAI+CH_3O-MBI mixture, (b) MBI, FAI, and FAI+MBI mixture, (c) Cl-MBI, FAI, and FAI+Cl mixture, (d) F-MBI, FAI, and FAI+F mixture.

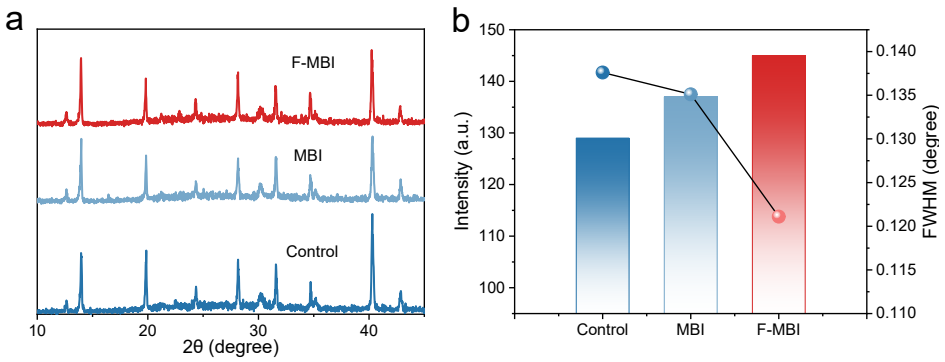

Fig. S8 (a) XRD patterns of control, MBI and F-MBI modified perovskite films. (b) The bar charts illustrate the variation in XRD peak intensity at 14.2° for the control, MBI, and F-MBI modified perovskite films, along with the corresponding FWHM values.

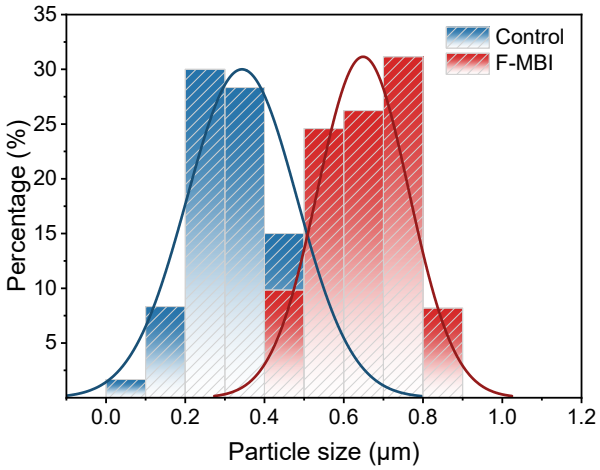

Fig. S9 Grain size distribution of the control and F-MBI modified perovskite films.

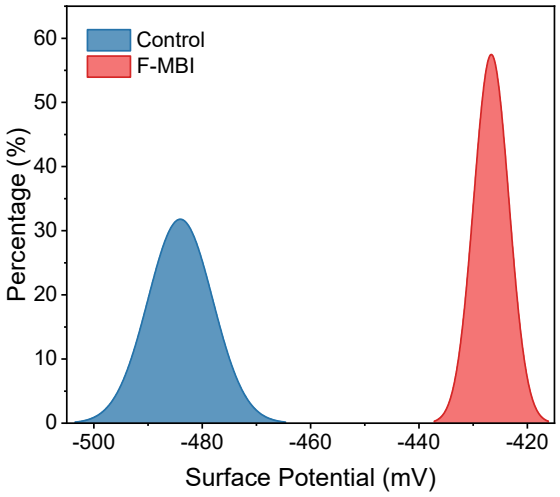

Fig. S10 Histograms of the CPD from the KPFM images for the control and F-MBI modified perovskite films.

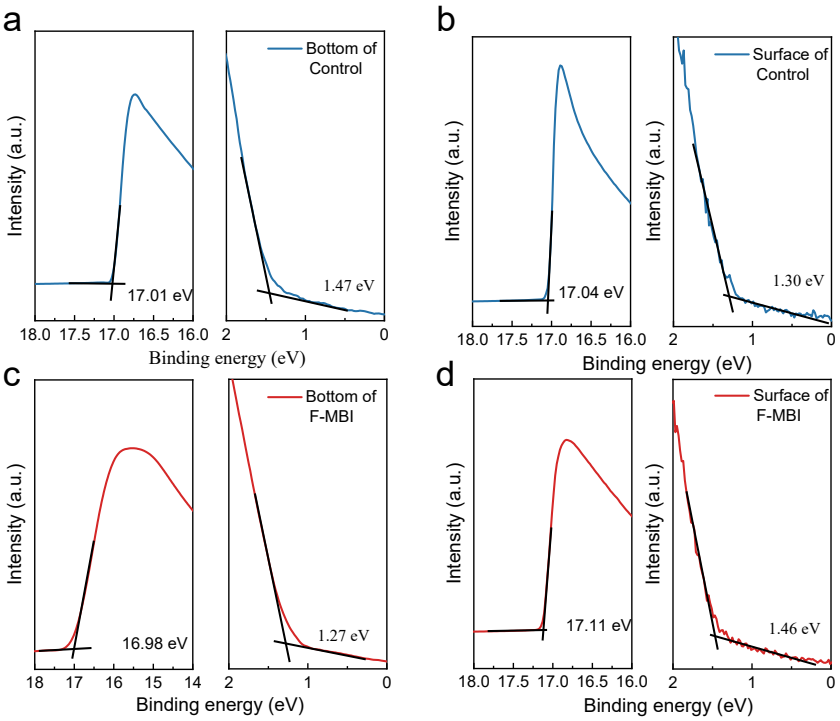

Fig. S11 UPS energy spectrum of (a) the buried interface and (b) surface of the control perovskite film, (c) the buried interface and (d) surface of the F-MBI modified perovskite film.

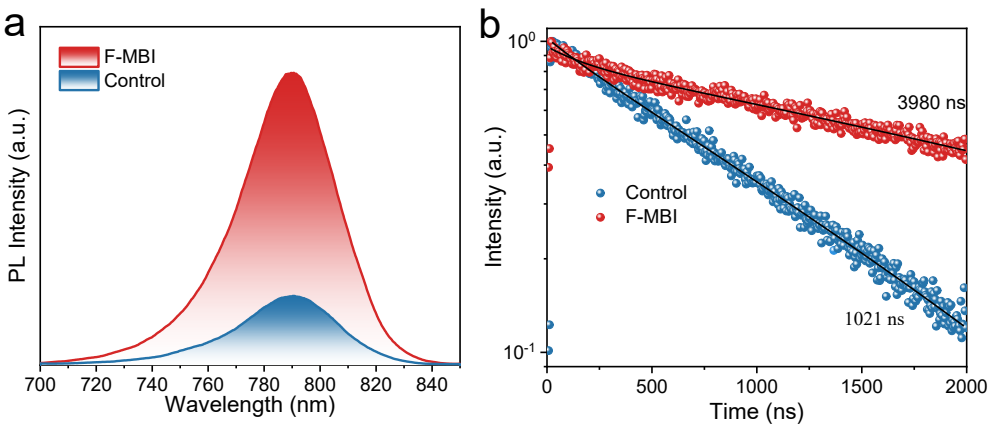

Fig. S12 (a) PL and (b) TRPL decay profiles of control and F-MBI modified perovskite film.

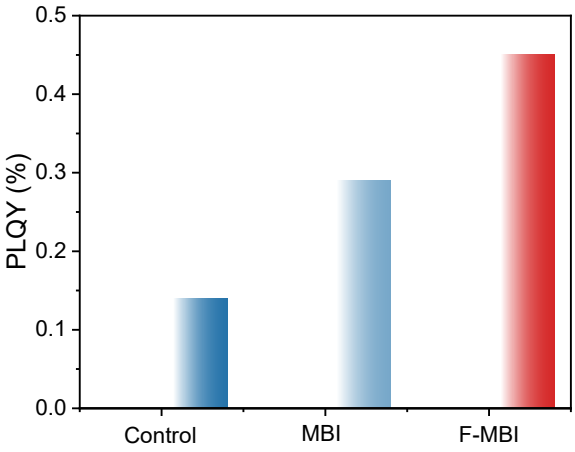

Fig. S13 PLQY of control and F-MBI modified perovskite films.

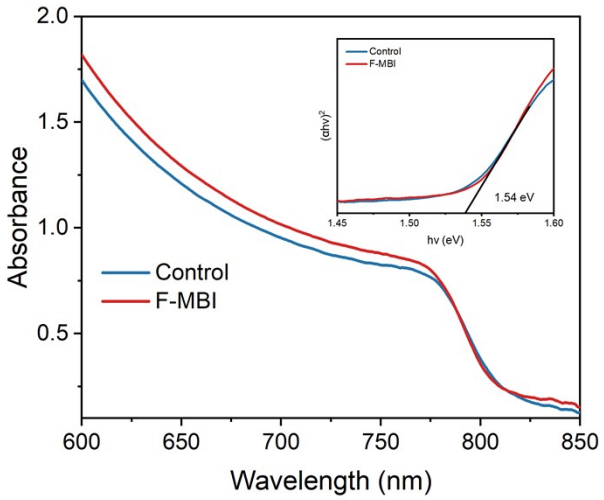

Fig. S14 Ultraviolet visible absorption spectra of perovskite films. The illustration is the T_{auc} plot for control and F-MBI modified perovskite films.

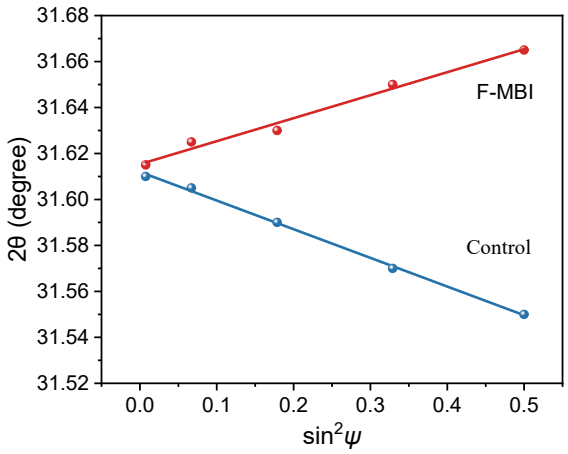

Fig. S15 The residual strain of the corresponding diffraction peaks (2θ) of control and F-MBI modified perovskite film as a function of $\sin^2\psi$.

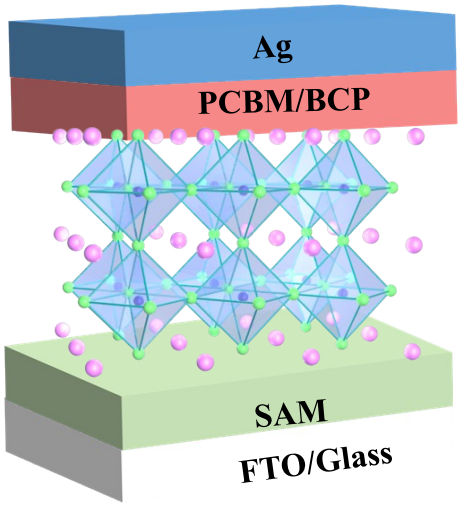

Fig. S16 Schematic of the PSC with the structure of FTO/SAM/perovskite/PCBM/BCP/Ag.

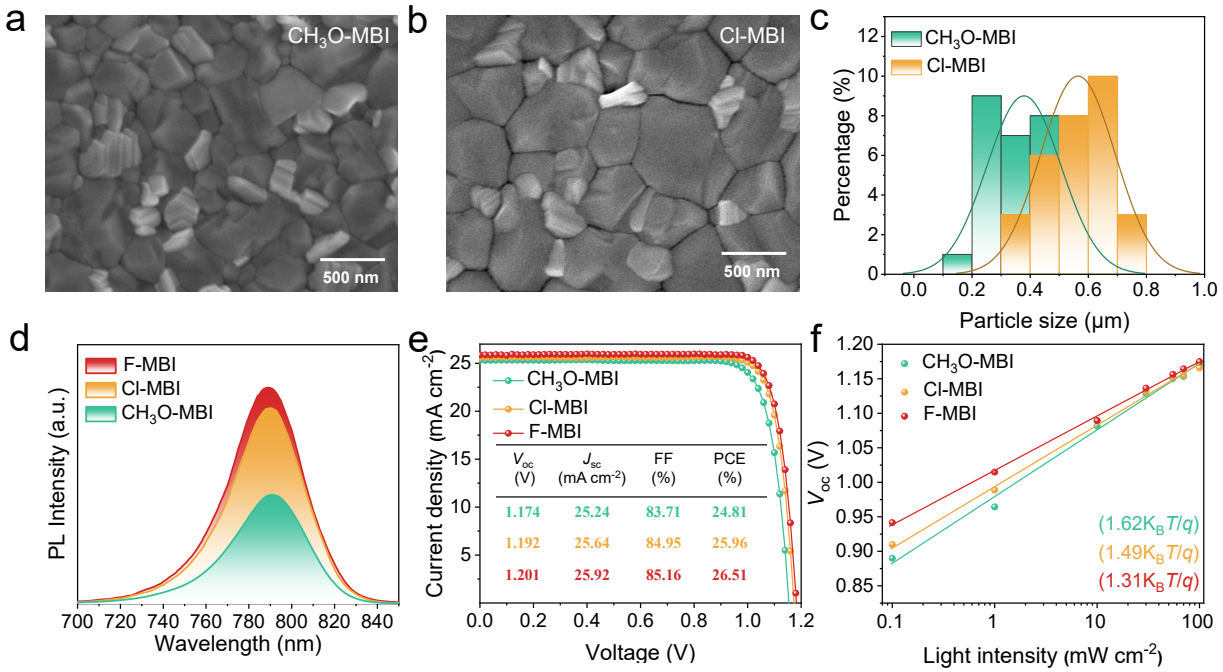

Fig. S17 Top-view SEM images of the (a) CH_3O-MBI and (b) Cl-MBI modified perovskite films. (c) Grain size distribution, (d) PL, (e) J-V curves under reverse scan directions and corresponding photovoltaic parameters and (f) V_{oc} curves versus light intensities of CH_3O-MBI, Cl-MBI and F-MBI modified perovskite films.

To further verify the consistency between experimental observations and theoretical predictions, the morphology and optoelectronic properties of perovskite films modified with CH_3O-MBI, Cl-MBI, and F-MBI were systematically compared. As shown in the SEM images (Fig. S17a-c), the average grain sizes of the CH_3O-MBI and Cl-MBI modified films are 0.37 μm and 0.56 μm, respectively, both smaller than that of the F-MBI modified film (0.65 μm), indicating that F-MBI promotes more complete crystallization and improved film uniformity. Correspondingly, the F-MBI modified perovskite exhibits stronger PL intensity and higher PCE compared with CH_3O-MBI and Cl-MBI (Fig. S17d-e), consistent with the theoretical prediction that fluorine substitution enhances electronic coupling and suppresses nonradiative pathways. Furthermore, the ideality factor (n) derived from the slope of the V_{oc}-light intensity plots (Fig. S17f) confirms that nonradiative recombination is effectively suppressed in the F-MBI based device. Overall, these results demonstrate that the superior performance of F-MBI arises from the synergistic

effect of its high electronegativity and low steric hindrance, which maximizes hydrogen-bonding strength, stabilizes the electronic structure and configuration of FA^+, and consequently enhances both the film quality and device stability and efficiency.

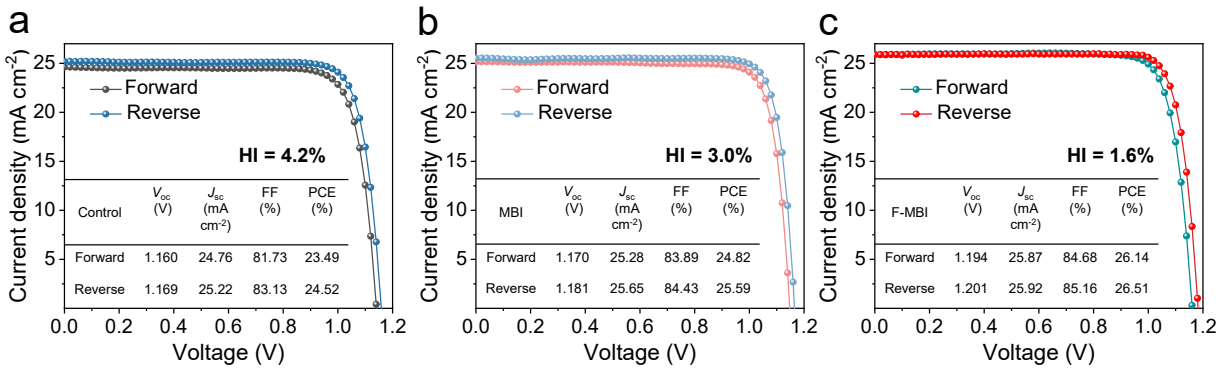

Fig. S18 *J-V* curves under forward and reverse scanning for (a) control (b) MBI and (c) F-MBI modified devices.

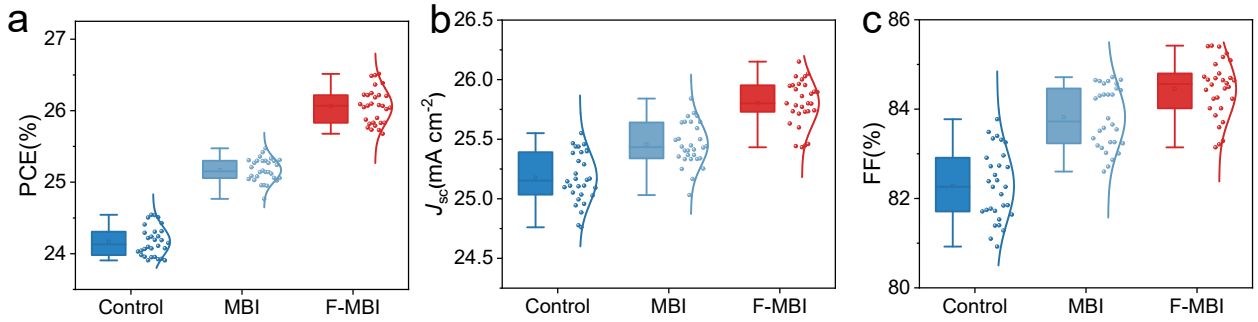

Fig. S19 Statistical distribution of optoelectronic parameters of PSCs based on control, MBI and F-MBI modified devices. (a) PCE (b) J_{sc} and (c) FF values obtained from 30 devices, respectively.

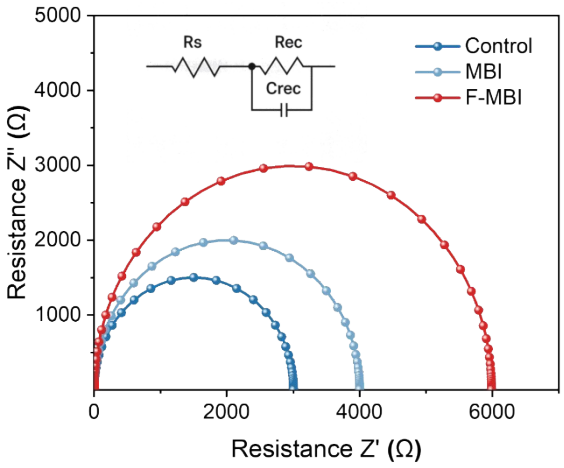

Fig.S20 The equivalent circuit models, Nyquist plots, and fitting curves obtained from the devices in dark.

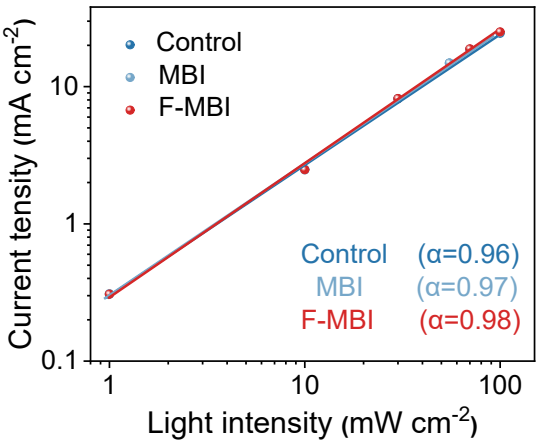

Fig. S21 Variation of J_{sc} of the control, MBI and F-MBI modified devices with light intensity.

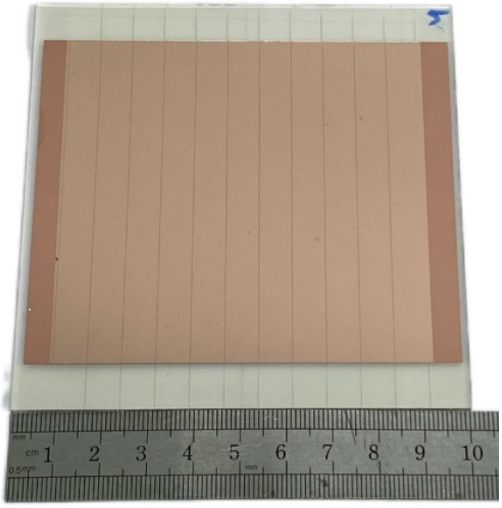

Fig. S22 Photo of large-area perovskite module.

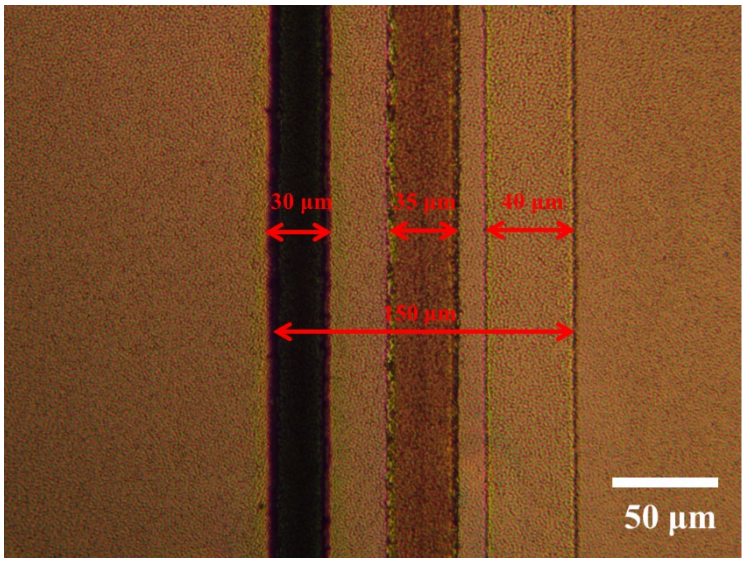

Fig. S23 The large-area modules laser etching lines morphology, P1, P2, P3 width and dead-area width.

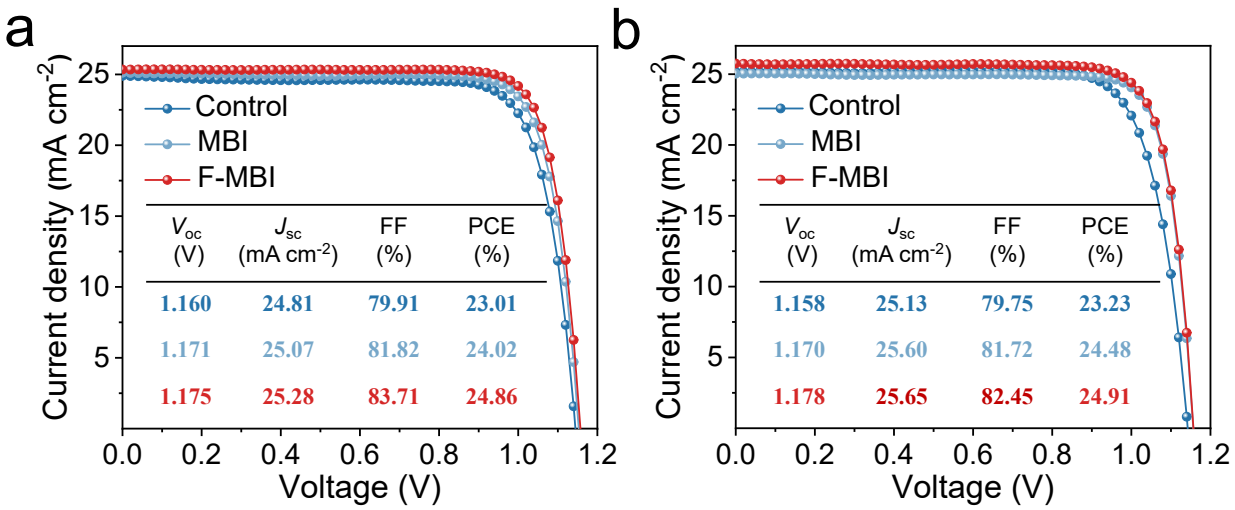

Fig. S24 *J-V* curves from the initial reverse scan of (a) the maximum power point tracking stability test and (b) the thermal stability test at 85 °C in N_2 for the control, MBI, and F-MBI modified devices. (Device structure: FTO/SAM/perovskite/PCBM/ALD SnO_2/Ag)

Table S1. The proton dissociation energies (PDEs) of FA^+ and R-MBI (R = CH_3O, Cl and F) composite systems were calculated using density functional theory (DFT).

Sample	Energy (kcal/mol)	Sample	Energy (kcal/mol)	H (kcal/mol)	PDEs (kcal/mol)
FA^+	-94170.26	FA^+-H	-93896.07	-263.55	10.64
CH_3O-MBI + FA^+	-653768.96	CH_3O-MBI + FA^+-H	-653477.13	-263.55	28.27
Cl-MBI + FA^+	-870316.72	Cl-MBI + FA^+-H	-870024.94	-263.55	28.22
F-MBI + FA^+	-644212.58	F-MBI + FA^+-H	-643920.25	-263.55	28.78

Table S2. Fitting carrier lifetimes of control and F-MBI modified perovskite films determined by TRPL.

Sample	A_1	τ_1 (ns)	A_2	τ_2 (ns)	τ_{ave} (ns)
Control	0.10	183.88	1.05	3997.32	1021
F-MBI	0.05	149.87	0.99	1021.71	3980

Table S3. Detailed photovoltaic parameters for the best performing perovskite solar cells (PSCs).

Device	Scanning	V_{oc} (V)	J_{sc} (mA cm^{-2})	FF (%)	PCE (%)	HI(%)
Control	Reverse	1.169	25.22	83.13	24.52	4.2
	Forward	1.160	24.76	81.73	23.49	
CH_3O-MBI	Reverse	1.166	25.19	81.48	23.94	3.5
	Forward	1.174	25.24	83.71	24.81	
MBI	Reverse	1.181	25.65	84.43	25.59	3.0
	Forward	1.170	25.28	83.89	24.82	
Cl-MBI	Reverse	1.181	25.41	84.71	25.41	2.1
	Forward	1.192	25.64	84.65	25.96	
F-MBI	Reverse	1.201	25.92	85.16	26.51	1.6
	Forward	1.194	25.87	84.86	26.14	

Table S4. Statistics of photovoltaic parameters for 30 individual PSCs.

Device	V_{oc} (V)	J_{sc} (mA cm^{-2})	FF (%)	PCE (%)
Control	1.166±0.004	25.156±0.395	82.349±1.426	24.225±0.319
MBI	1.181±0.007	25.436±0.405	83.658±1.056	25.120±0.353
F-MBI	1.196±0.007	25.792±0.360	84.282±1.138	26.095±0.418

Table S5. Defect density (N_t) calculated by SCLC of control, MBI and F-MBI modified PSCs.

Device	Structure	N_t (cm^{-3})
Control	Hole-only	1.60×10^{15}
MBI	Hole-only	1.28×10^{15}
F-MBI	Hole-only	1.07×10^{15}

Table S6. The photovoltaic parameters of the control and F-MBI modified modules.

Device	Scan direction	V_{oc} (V)	J_{sc} (mA cm^{-2})	FF (%)	PCE (%)
control	RS	11.39	2.16	74.83	18.46
F-MBI	RS	12.40	2.173	77.86	20.99

Table S7. Comparisons of stability test in high-performance IPSCs based on rigid substrates.

Device champion PCE (%)	Aging conditions and corresponding stability	Ref.
26.81%	Unencapsulated, 1 sun illumination, 30 °C, N_2, 2000 h; 95.8% normalized PCE.	8
24.5%	Encapsulation, 1 sun illumination, 30 °C, N_2, 2060 h; 98% absolute PCE.	9
25.35%	Unencapsulated, 1 sun illumination, 60 °C, N_2, 1000 h; 92.8% absolute PCE. Unencapsulated, 85 °C, N_2, 800h; 91.7% absolute PCE	10
26.15%	Unencapsulated, 1 sun illumination, 65 °C, N_2, 1000 h; 94.2% normalized PCE. Unencapsulated, 85 °C, N_2, 500 h; 90.4% normalized PCE	11
25.01%	Unencapsulated, 1 sun illumination, 65 °C, N_2, 800 h; 90% normalized PCE. Unencapsulated, 65 °C, N_2, 1000 h; 91% normalized PCE.	12
25%	Unencapsulated, 1 sun illumination, 30 °C, N_2, 500 h; 95% normalized PCE. Unencapsulated, 85 °C, N_2, 500 h; 82% normalized PCE.	13
26%	Unencapsulated, 1 sun illumination, 65 °C, N_2, 1000 h; 95.4% normalized PCE.	14
25.2%	Unencapsulated, 85 °C, N_2, 1000 h; 90% normalized PCE.	15
25.45%	Unencapsulated, 1 sun illumination, 30 °C, N_2, 3000 h; 82% absolute PCE. Unencapsulated, 85 °C, N_2, 1000 h; 90% absolute PCE.	16
25.03%	Unencapsulated, 1 sun illumination, 65 °C, N_2, 1000 h; 90% normalized PCE.	17

26.67%	Unencapsulated, 1 sun illumination, 65 °C, N_2, 1700 h; 93% normalized PCE.	18
24.1%	Unencapsulated, 1 sun illumination, 85 °C, N_2, 1500 h; 90% absolute PCE.	19
25.35%	Unencapsulated, 1 sun illumination, 40 °C, N_2, 700 h; 90% normalized PCE. Unencapsulated, 85 °C, N_2, 1000 h; 93% absolute PCE.	20
25.56%	Unencapsulated, 1 sun illumination, 65 °C, N_2, 1000 h; 80% normalized PCE.	21
26.51%	**Unencapsulated, 1 sun illumination, 65 °C, N_2, 1950 h; 90% absolute PCE. Unencapsulated, 85 °C, N_2, 816 h; 90% absolute PCE.**	**This work**

References

1 Y. Han, J. Liu, P. Wang, H. Ma, R. Cai, M. Wang, J. Bian and Y. Shi, *ACS Appl. Mater. Interfaces*, 2024, **16**, 39312–39320.

2 R. Tian, C. Liu, Y. Meng, Y. Wang, R. Cao, B. Tang, D. Walsh, H. Do, H. Wu, K. Wang, K. Sun, S. Yang, J. Zhu, X. Li and Z. Ge, *Adv. Mater.*, 2024, **36**, 2309998.

3 J. Wang, S. Hu, H. Zhu, S. Liu, Z. Zhang, R. Chen, J. Wang, C. Shi, J. Zhang, W. Liu, X. Lei, B. Liu, Y. Pan, F. Ren, H. Raza, Q. Zhou, S. Li, L. Qiu, G. Zheng, X. Qin, Z. Zhao, S. Yang, N. Li, J. Li, A. Wakamiya, Z. Liu, H. J. Snaith and W. Chen, *Nat. Commun.*, 2025, **16**, 4917.

4 M. Li, R. Sun, J. Chang, J. Dong, Q. Tian, H. Wang, Z. Li, P. Yang, H. Shi, C. Yang, Z. Wu, R. Li, Y. Yang, A. Wang, S. Zhang, F. Wang, W. Huang and T. Qin, *Nat. Commun.*, 2023, **14**, 573.

5 T. D. W. Claridge, *High-resolution NMR techniques in organic chemistry*, Elsevier, 2016.

6 Y. Wang, C. Lu, M. Liu, C. Zhu, J. Zhang, S. Qin, Z. Liu, M. Liu, Y. Zhao, F. Wang, X. Li, L. Meng and Y. Li, *Nat. Photonics*, 2025, **19**, 985–991.

7 J. Ye, W. Sheng, J. He, Y. Zhong, Y. Liu, K. Liu, L. Tan and Y. Chen, *Angew. Chem. Int. Ed.*, 2024, **63**, e202411708.

8 M. Lu, J. Ding, Q. Ma, Z. Zhang, M. Li, W. Gao, W. Mo, B. Zhang, T. Pauporté, J. Zhang, Y. Wang, J.-X. Tang, J. Chen and C. Chen, *Energy Environ. Sci.*, 2025, **18**, 5973–5984.

9 N. Li, Z. Shi, C. Fei, H. Jiao, M. Li, H. Gu, S. P. Harvey, Y. Dong, M. C. Beard and J. Huang, *Nat. Energy*, 2024, **9**, 1264–1274.

10 Y. Zheng, C. Tian, X. Wu, A. Sun, R. Zhuang, C. Tang, Y. Liu, Z. Li, B. Ouyang, J. Du, Z. Li, X. Wu, J. Chen, J. Cai and C. Chen, *Adv. Energy Mater.*, 2024, **14**, 2304486.

11 Y. Zheng, Y. Li, R. Zhuang, X. Wu, C. Tian, A. Sun, C. Chen, Y. Guo, Y. Hua, K. Meng, K. Wu and C.-C. Chen, *Energy Environ. Sci.*, 2024, **17**, 1153–1162.

12 Z. Cui, W. Li, B. Feng, Y. Li, X. Guo, H. Yuan, Q. Weng, T. You, W. Zhang, X. Li and J. Fang, *Adv. Mater.*, 2024, **36**, 2410273.

13 J. Liu, J. Chen, L. Xie, S. Yang, Y. Meng, M. Li, C. Xiao, J. Zhu, H. Do, J. Zhang, M. Yang and Z. Ge, *Angew. Chem. Int. Ed.*, 2024, **63**, e202403610.

14 M. Chen, Z. Qin, Z. Zhang, W. Xiang, Y. Liu, C. Tian, S. Chen, Y. Wang and L. Han, *Nat. Commun.*, 2025, **16**, 5746.

15 X. Wang, J. Li, R. Guo, X. Yin, R. Luo, D. Guo, K. Ji, L. Dai, H. Liang, X. Jia, J. Chen, Z. Jia, Z. Shi, S. Liu, Y. Wang, Q. Zhou, T. Wang, G. Pan, P. Müller-Buschbaum, S. D. Stranks and Y. Hou, *Nat. Photonics*, 2024, **18**, 1269–1275.

16 H. Xu, Z. Liang, J. Ye, Y. Zhang, Z. Wang, H. Zhang, C. Wan, G. Xu, J. Zeng, B. Xu, Z. Xiao, T. Kirchartz and X. Pan, *Energy Environ. Sci.*, 2023, **16**, 5792–5804.

17 B. Tuo, Z. Wang, Z. Ren, H. Zhang, X. Lu, Y. Zhang, S. Zang and Y. Song, *Energy Environ. Sci.*, 2024, **17**, 2945–2955.

18 Z. Lv, Z. Wang, G. Liu, Y. Gao, S. Li, Z. Liu, M. Xu, J. Cheng, W. Zhao, W. Lu, P. Wang, J. Wei, M. Wang, W. Tian, W. Li, Y. Yan, J. Bian and Y. Shi, *Adv. Mater.*, 2025, e13600.

19 M. Wang, Z. Shi, C. Fei, Z. J. D. Deng, G. Yang, S. P. Dunfield, D. P. Fenning and J. Huang, *Nat. Energy*, 2023, **8**, 1229–1239.

20 H. Meng, K. Mao, F. Cai, K. Zhang, S. Yuan, T. Li, F. Cao, Z. Su, Z. Zhu, X. Feng, W. Peng, J. Xu, Y. Gao, W. Chen, C. Xiao, X. Wu, M. D. McGehee and J. Xu, *Nat. Energy*, 2024, **9**, 536–547.

21 S. Wang, W. Tian, Z. Cheng, X. Shi, W. Fan, J. Zhou, D. Gu, J. Xue and R. Wang, *Nat. Energy*, 2025, **10**, 1074–1083.